A Novel Phase-Shift Pulsewidth Modulation Method for Light-Load Bidirectional *CLLC* Resonant Converter

Yuzhen Xu, Xiangyang Dai, Zhongyi Zhang, Zhiwei Kang, and Tao Jin, *Senior Member, IEEE*

***Abstract*—For the bidirectional full-bridge *CLLC* resonant converter, soft switching of primary side and secondary side switches and bidirectional power transmission are its obvious advantages. However, in the pulse frequency modulation control under light-load conditions, the converter will have the disadvantages of output voltage imbalance and low transmission efficiency. In order to improve the range of voltage regulation and efficiency of *CLLC* resonant converter under light-load conditions, a novel phase-shift pulsewidth modulation method is proposed in this article. There is low voltage gain regulation and low operation losses can be achieved under light load. Considering the parasitic parameters and dead time of the switches, the voltage gain of the proposed control method under light load is precise research by using the time domain analysis method. Finally, an experimental prototype of a bidirectional full-bridge *CLLC* resonant converter with 200 V input voltage, 200 V output voltage, and a rated power of 800 W is designed. According to the simulation and experimental results, it can be shown that the proposed control method is effective under light-load operation.**

***Index Terms*—*CLLC* resonant converter, light load, phase-shift pulsewidth modulation (PS-PWM), precise research of gain, time domain analysis method.**

NOMENCLATURE

PFM	Pulse frequency modulation.
PWM	Pulsewidth modulation.
APWM	Asymmetrical pulsewidth modulation.
PS-PWM	Phase-shift pulsewidth modulation.
FHA	Fundamental harmonic analysis.
ZVS	Zero voltage switching-ON.
ZCS	Zero current switching-OFF.
f_s	Switching frequency.
f_r	Resonant frequency.
V_{in}	Input voltage.
V_{o}	Output voltage.
RTM	Resonant tank module.
u_{ab}	Input port ac voltage of RTM.
$u_{\mathrm{cd'}}$	Output port ac voltage of RTM.
k	Inductance ratio.
g	Capacitance ratio.
L_{m}	Magnetizing inductance.
L_{r1} and L_{r2}	Resonant inductor.
C_{r1} and C_{r2}	Resonant capacitor.
R_{o}	Rated load resistance.
C'_{oss}	Switches parasitic capacitances value.
$i_{L\mathrm{r1}}$	Primary resonance current.
$i_{L\mathrm{m}}$	*TX* exciting current.
$i_{L\mathrm{r2}}$	Secondary resonance current.
i_{o}	Output current.
f_{n}	Normalized frequency.
R_{eq}	AC equivalent resistance.
Z_{r}	Characteristic impedance.
Q	Quality factor.
n	Transformer turn ratio.
D_{s}	Switches duty ratio.
T_{d}	Dead time of switches.

I. INTRODUCTION

With the rapid rise of distributed renewable energy generation, in the fields of electric vehicles, energy storage systems, bidirectional isolated dc–dc converter has become a new research hotspot [1], [2], [3], [4], [5], [6]. The bidirectional *LLC* converter can realize ZVS and ZCS in a large frequency range [7], [8]. However, due to the asymmetry of circuit structure, it is equivalent to a series resonant circuit in reverse operation, and the gain is less than 1, which is not suitable for a large voltage regulation range. Therefore, the work in [9] and [10] proposed a bidirectional *CLLC* resonant converter, on the basis of the original bidirectional *LLC* converter, a set of *LC* devices were added at the secondary side of the transformer, so that the working characteristics of the converter were completely consistent when it worked forward or reversely. Its advantage is that the voltage can be lifted and lowered in two-way operation, and the soft switching can be realized in a large frequency range. So it has a great advantage in high voltage, high frequency, and high power applications [11], [12].

Manuscript received 16 April 2022; revised 29 June 2022 and 7 September 2022; accepted 17 October 2022. Date of publication 25 October 2022; date of current version 26 December 2022. This work was supported in part by the Chinese National Natural Science Foundation under Grant 51977039 and in part by the Central Government Guiding Local Science and Technology Development Project under Grant 2021L3005. Recommended for publication by Associate Editor G. Grandi. *(Corresponding author: Tao Jin.)*

The authors are with the Department of Electrical Engineering, Fuzhou University, Fuzhou 350116, China (e-mail: xyz@fzu.edu.cn; 3479300060@qq.com; zhangfzu1993@qq.com; 463450661@qq.com; jintly@fzu.edu.cn).

Color versions of one or more figures in this article are available at https://doi.org/10.1109/TPEL.2022.3217104.

Digital Object Identifier 10.1109/TPEL.2022.3217104

The control of *CLLC* converter is usually based on the PFM method. With the increase of f_s, its voltage gain decreases and equals 1 at the resonant frequency. However, when the circuit works under light-load conditions, due to the influence of the parasitic capacitance of the switches on the output side, the voltage gain will increase with the increase of the f_s after the f_s is greater than the resonance frequency [13], [14], [15], [16]. Therefore, the traditional PFM cannot effectively realize the low voltage gain under the condition of light load, and the high f_s will also reduce the transmission efficiency.

In order to flexibly adjust the voltage gain while maintaining high efficiency under light load, and keeping the output voltage constant when the load changes, a variety of control methods have been proposed [17], [18], [19], [20], [21], [22], [23]. The work in [17] and [18] mainly described the burst-mode control, which modulates the light-load voltage by periodically skipping the switching pulse, but this method will cause a larger output voltage ripple. Fang et al. [19] proposed an energy feedback control in which the output-side rectifier transfers energy from the load to the power supply, to reduce the output voltage of the converter at light load, but it also leads to low efficiency. In [20], the PWM control method for *LLC* converters was proposed, which expanded the output voltage range by changing the duty cycle of the drive signal, but the duty cycle is limited by the soft switching, so the voltage gain is still limited. Different from the conventional PWM method, the APWM method was proposed [21], [22]. The output voltage is reduced by reducing the equivalent duty cycle of the RTM input, and the soft switching can be realized in the primary and secondary sides. However, the APWM method will lead to larger resonant current and larger switching losses of the switches. Shakib and Mekhilef [23] proposed a new control method. It is that combining the adaptive frequency control and phase shift control, the ZVS of the primary side switches and the effective regulation of the output voltage can be realized in the load switching and wide input voltage range. But it can only be applied to transformers with central taps and forward resonant converters.

In order to improve the voltage gain regulation ability and efficiency of the *CLLC* resonant converter under light-load conditions, a novel PS-PWM control method is proposed. In this control method, through the phase shift and variable duty cycle of the primary side switches at the same time, while reducing the equivalent duty cycle of the RTM input to reduce the voltage gain, the current stress is small to reduce the switching loss of the device. Both the primary and secondary switches of the circuit can realize ZVS and have high light-load efficiency. By using the time domain analysis method [24], [25], [26], the voltage gain expression under this control method is derived under the premise of considering the parasitic parameters and dead time. Finally, an experimental prototype with an input voltage of 200 V, an output voltage of 200 V, and a rated power of 800 W is built for experimental verification. It is proved that the proposed novel PS-PWM control method has a good low voltage gain adjustment ability and high efficiency of the bidirectional full-bridge *CLLC* resonant converter under light-load condition.

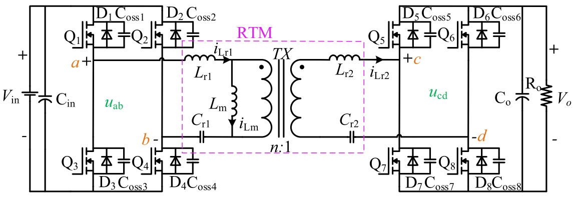

Fig. 1. Configuration of full-bridge *CLLC* resonant converter.

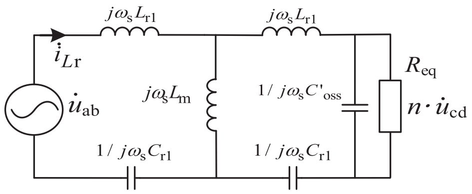

Fig. 2. AC equivalent operation circuit.

The rest of the article is organized as follows. In Section II, the traditional PFM is described and the light-load characteristics are analyzed. In Section III, the proposed modulation method is described and analyzed, and the gain function under this control is derived. In Section IV, the simulation experiment is carried out according to the proposed modulation method. Section V discusses the prototype experiment results. Finally, Section VI concludes the article.

II. ANALYSIS OF PFM CONTROL CHARACTERISTICS

The circuit structure of the bidirectional full bridge *CLLC* resonant converter is shown in Fig. 1, which is composed of an inverter, a rectifier, and a symmetrical RTM on the primary and secondary sides. L_m is the magnetizing inductance of the transformer, L_{r1} and L_{r2} are the primary and secondary resonant inductances, which contain the leakage inductance of the primary and secondary sides of the transformer, C_{r1} and C_{r2} are the primary and secondary resonant capacitors. Because the parameter structure of the RTM is symmetrical, then $L_{r1} = n^2 L_{r2}$, $C_{r1} = C_{r2}/n^2$.

PFM control adjusts the output voltage gain by adjusting the f_s of the switches. When the converter is working in the forward mode, two almost 0.5 duty cycle complementary PWM drive signals are applied to Q_1, Q_4 and Q_2, Q_3, respectively, to make full bridge inverter output ac square wave. Meanwhile, there is no drive signal to Q_5–Q_8, and the body diodes of Q_5–Q_8 are used to form a full-bridge rectifier circuit to circulate the output current i_{Lr2} of RTM; Similarly, when the converter works in reverse, drive signals are applied to Q_5, Q_8 and Q_6, Q_7, respectively, and Q_1–Q_4 form a rectifier circuit at the same time. In this article, the influences of the parasitic capacitance of the output side switches on the voltage gain under light load are analyzed based on the FHA method. When the *CLLC* resonant converter works under light load, the fundamental equivalent circuit included parasitic capacitance of the output side switches is shown in Fig. 2, where C'_{oss} is the parasitic capacitance of the output side switches, $\dot{u}_{ab}$ is the fundamental frequency component of the terminal voltage, and $\dot{u}_{cd}$ is the fundamental frequency component of the terminal voltage.

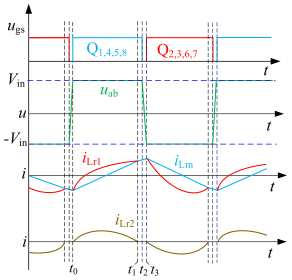

Fig. 3. Under-resonant mode waveforms.

Then, the transfer function of the RTM can be derived as

$$G\left(j\omega_{\mathrm{s}}\right)=\frac{\dot{u}_{\mathrm{cd}}\pi/4n}{\dot{u}_{\mathrm{ab}}\pi/4}$$

$$=\frac{j\omega_{\mathrm{s}}L_{\mathrm{m}}//(j\omega_{\mathrm{s}}L_{\mathrm{r1}}-j/\omega_{\mathrm{s}}C_{\mathrm{r1}}+R_{\mathrm{eq}}//j/\omega_{\mathrm{s}}C'_{\mathrm{oss}})}{j\omega_{\mathrm{s}}L_{\mathrm{r1}}-j/\omega_{\mathrm{s}}C_{\mathrm{r1}}+j\omega_{\mathrm{s}}L_{\mathrm{m}}//(j\omega_{\mathrm{s}}L_{\mathrm{r1}}-j/\omega_{\mathrm{s}}C_{\mathrm{r1}}+R_{\mathrm{eq}}//j/\omega_{\mathrm{s}}C'_{\mathrm{oss}})}$$

$$\frac{R_{\mathrm{eq}}//j/\omega_{\mathrm{s}}C'_{\mathrm{oss}}}{j\omega_{\mathrm{s}}L_{\mathrm{r1}}-j/\omega_{\mathrm{s}}C_{\mathrm{r1}}+R_{\mathrm{eq}}//j/\omega_{\mathrm{s}}C'_{\mathrm{oss}}} \tag{1}$$

where ω_{s} is the switching angular frequency.

Using (1), the gain G (f_{n}, k, Q, g) can be reformulated with the normalized frequency f_{n} as follows [12]:

$$G(f_{\mathrm{n}},k,Q,g)=\left|G\left(j\omega_{\mathrm{s}}\right)\right|$$

$$=\frac{1}{\sqrt{\begin{array}{l}\left[f_{\mathrm{n}}^{2}\left(-2g-\frac{g}{k}\right)+1+\frac{1}{k}+2g+\frac{2g}{k}-\frac{1+g}{f_{\mathrm{n}}^{2}k}\right]^{2}\\+\left[f_{\mathrm{n}}Q\left(2+\frac{1}{k}\right)+\frac{2Q}{f_{\mathrm{n}}}\left(-1-\frac{1}{k}+\frac{1}{2f_{\mathrm{n}}^{2}k}\right)\right]^{2}\end{array}}} \tag{2}$$

where the key parameters f_{n}, k, R_{eq}, g, and Q are specifically expressed as

$$\begin{cases}f_{\mathrm{n}}=\frac{f_{\mathrm{s}}}{f_{\mathrm{r}}};\omega_{\mathrm{r}}=\frac{1}{\sqrt{L_{\mathrm{r1}}C_{\mathrm{r1}}}};Z_{\mathrm{r}}=\sqrt{\frac{L_{\mathrm{r1}}}{C_{\mathrm{r1}}}}\\Q=\frac{Z_{\mathrm{r}}}{R_{\mathrm{eq}}};k=\frac{L_{\mathrm{m}}}{L_{\mathrm{r1}}};R_{\mathrm{eq}}=\frac{8n^{2}R_{o}}{\pi^{2}};g=\frac{C'_{\mathrm{oss}}}{C_{\mathrm{r1}}}.\end{cases} \tag{3}$$

According to the value of f_{n}, *CLLC* working modes can be divided into three types: Mode 1 is an under-resonant state, $f_{\mathrm{n}}<1$ and $G>1$; Mode 2 is a fully resonant state, $f_{\mathrm{n}}=1$ and $G=1$; Mode 3 is an over-resonant state, $f_{\mathrm{n}}>1$ and $G<1$. The working waveforms in the under-resonant mode are shown in Fig. 3.

When the circuit is working under light load or no-load, some important devices that cannot be shut down at will, such as server power supply, have to minimize the output voltage to reduce the loss of the device. At this time, the resonant circuit should work in Mode 3: $G<1$. The circuit needs to reduce the output voltage by increasing the operating frequency, which will increase the switching loss of the converter. And due to the parasitic capacitance of the output side switches, the resonant converter will produce gain distortion at high frequency. When $k=4$ and $g=0.003$, the gain curve G (f_{n}, Q) according to (2) is shown in Fig. 4(a), where the value of k refers to $k=4.3$ as like as [12], and the value of g is also estimated by the resonant capacitance value [12] and the parasitic capacitance value of actual commonly used switches. It can be seen that the load becomes lighter and the voltage gain distortion becomes more serious. Therefore, the voltage gain cannot be flexibly adjusted by using PFM control under light load.

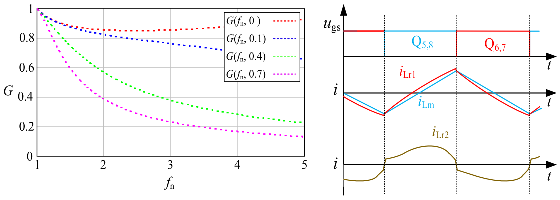

(a) (b)

Fig. 4. (a) Gain curve of *CLLC* resonant converter. (b) Over-resonant mode waveforms under light load.

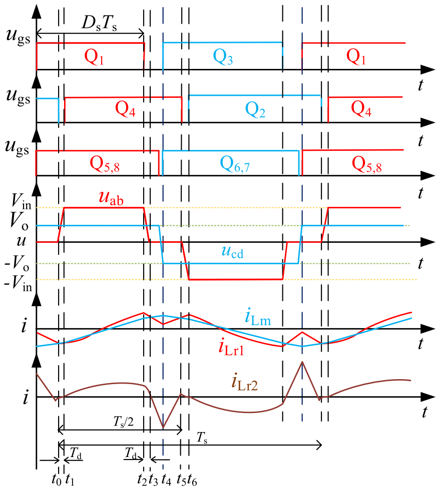

Fig. 5. PS-PWM operation waveforms.

When the resonant converter operates in the under-resonant region, as shown in Fig. 3, i_{Lr1} will be equaled to i_{Lm} for a period of time, and i_{Lm} refers to the current flowing through the primary excitation inductance of the transformer [14]. According to Kirchhoff's current law, i_{Lr2} is zero and the secondary body diodes can realize ZCS. When the operating frequency is in the over-resonant region, since $f_{\mathrm{s}}>f_{\mathrm{r}}$, the phenomenon that i_{Lr1} equals i_{Lm} disappears. As shown in Fig. 4(b), the secondary body diodes cannot achieve complete ZCS.

III. OPERATING CHARACTERISTICS OF A NOVEL PS-PWM CONTROL

A. *Operating Principles of the Proposed Novel PS-PWM Method*

In order to effectively adjust the low gain of the circuit under light-load conditions, a novel PS-PWM control is proposed, whose key waveforms are shown in Fig. 5. The duty cycle of Q_1 and Q_3 is D_{s} ($0.25\leq D_{\mathrm{s}}\leq 0.5$) and of Q_2 and Q_4 is almost 0.5. Q_4 lags Q_1 conduction, Q_2 lags Q_3 conduction, and Q_2, Q_4 complementary conduction. The switches of the output side are all driven by a symmetrical signal (the duty cycle are almost 0.5), and $Q_{5,8}$, $Q_{6,7}$ complementary conduction.

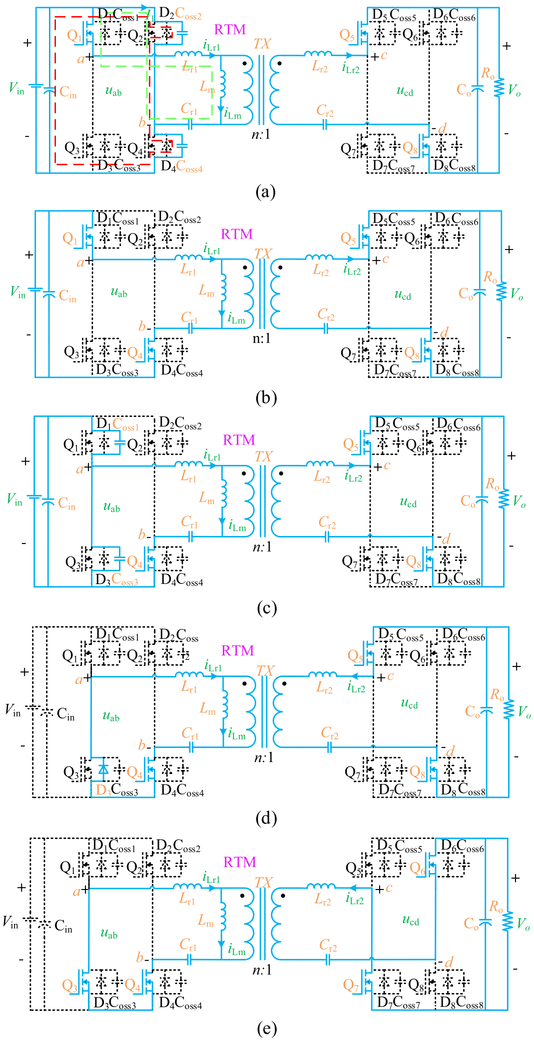

Fig. 6. Equivalent circuits of the converter. (a) State I [t_0, t_1]. (b) State II [t_1, t_2]. (c) State III [t_2, t_3]. (d) State IV [t_3, t_4]. (e) State V [t_4, t_5].

Using the optimization processing thought in the fundamental analysis method, three assumptions were established. First, the resonant current equals to the excitation current at the end of dead zone t_3. Second, the leading arm dead zone realizes critical zero voltage turn-ON, and the resonant current of the lagging arm dead zone is approximately equal to the excitation current, but it does not affect the clamping of L_{m}. Third, the resonant current is approximately symmetric at t_3–t_5 and $i_{Lr1}(t_3)$ equals to $i_{Lr1}(t_5)$. The dead time of lag arm is the same as that of advanced arm. Each state of the transient process in half-period based on Fig. 5 is analyzed as followed based on the whole key states of equivalent circuits that are plotted as shown in Fig. 6.

1) State I [t_0, t_1]: In Fig. 6(a), the switch Q$_2$ is turned OFF, Q$_1$, Q$_5$, and Q$_8$ are turned ON, but Q$_4$ is not yet turned ON at t_0. The C$_{\mathrm{oss2}}$ is charging and the C$_{\mathrm{oss4}}$ is discharging. At this point, the value of u_{ab} is V_{in}–V_{Coss4}, i_{Lr1} and i_{Lm} begin to increase. Q$_5$ and Q$_8$ are turned ON, the value of u_{cd} is clamped in V_{o}. The power is transferred from the output side to the input side, and the duration is T_{d}. According to the red line path and green line path of the primary current in Fig. 6(a), formula (4) can be obtained by Kirchhoff's law. Formula (5) also can be obtained by eliminating intermediate variable current I_1

$$\begin{cases} -\frac{V_{\mathrm{in}}}{s}+\frac{v_{\mathrm{ds4}}(t_0)}{s}+\frac{I_1}{sC_{\mathrm{oss2}}}+(I_1-i_{Lr1}(s))\frac{1}{sC_{\mathrm{oss4}}}=0\\ \frac{v_{Cr1}(t_0)}{s}-L_{\mathrm{r1}}i_{Lr1}(t_0)+\frac{nV_{\mathrm{o}}}{2s}+\left(\frac{1}{sC_{\mathrm{r1}}}+sL_{\mathrm{r1}}\right)i_{Lr1}(s)\\ +(i_{Lr1}(s)-I_1)\frac{1}{sC_{\mathrm{oss4}}}=0.\end{cases} \tag{4}$$

And $v_{\mathrm{ds4}}(t_0)$ equals to V_{in}, so

$$i_{Lr1}(t)=i_{Lr1}(t_0)\cos\left[\omega_1(t-t_0)\right]-\frac{(2v_{Cr1}(t_0)+nV_{\mathrm{o}})}{2Z_1}\sin\left[\omega_1(t-t_0)\right]. \tag{5}$$

The expression of i_{Lm} is

$$i_{Lm}(t)=\frac{nV_{\mathrm{o}}(t-t_0)}{2L_{\mathrm{m}}}+i_{Lm}(t_0) \tag{6}$$

where

$$Z_1=\sqrt{\frac{L_{\mathrm{r1}}(C_{\mathrm{r1}}+2C_{\mathrm{oss}})}{2C_{\mathrm{oss}}C_{\mathrm{r1}}}},\omega_1=\sqrt{\frac{C_{\mathrm{r1}}+2C_{\mathrm{oss}}}{2C_{\mathrm{oss}}C_{\mathrm{r1}}L_{\mathrm{r1}}}}. \tag{7}$$

C$_{\mathrm{oss}}$ is parasitic capacitance of switches.

2) State II [t_1, t_2]: In Fig. 6(b), switch Q$_4$ is turned ON at t_1. The voltage value of C$_{\mathrm{oss4}}$ has been discharged to zero, so Q$_4$ is realized ZVS. At this point, the value of u_{ab} is V_{in}, i_{Lr1} and i_{Lm} continue to increase. The power is transferred from the input side to the output side, and according to Kirchhoff's law, i_{Lr1} is written as

$$-\frac{V_{\mathrm{in}}}{s}+\frac{v_{Cr1}(t_1)}{s}-L_{\mathrm{r1}}i_{Lr1}(t_1)+\frac{nV_{\mathrm{o}}+V_{\mathrm{in}}}{2s}+\left(\frac{1}{sC_{\mathrm{r1}}}+sL_{\mathrm{r1}}\right)i_{Lr1}(s)=0. \tag{8}$$

So, we obtain

$$i_{Lr1}(t)=i_{Lr1}(t_1)\cos\left[\omega_2(t-t_1)\right]+\frac{V_{\mathrm{in}}-2v_{Cr1}(t_1)-nV_{\mathrm{o}}}{2Z_2}\sin\left[\omega_2(t-t_1)\right]. \tag{9}$$

The expression of i_{Lm} is

$$i_{Lm}(t)=\frac{V_{\mathrm{in}}(t-t_1)}{L_{\mathrm{m}}}+i_{Lm}(t_1) \tag{10}$$

where

$$Z_2=\sqrt{\frac{L_{\mathrm{r1}}}{C_{\mathrm{r1}}}},\omega_2=\sqrt{\frac{1}{C_{\mathrm{r1}}\cdot L_{\mathrm{r1}}}}. \tag{11}$$

3) State III [t_2, t_3]: In Fig. 6(c), Q$_1$ is turned OFF at t_2, and C$_{\mathrm{oss1}}$ is charging. The value of u_{ab} is V_{in}–V_{Coss1}, and u_{cd} is still clamped at V_{o}. The value of i_{Lr1} begins to decrease, and the increase rate of i_{Lm} decreases. According to Kirchhoff's law, i_{Lr1} is written as

$$\begin{cases} -\frac{V_{\mathrm{in}}}{s}+\frac{v_{\mathrm{ds3}}(t_2)}{s}+\frac{I_1}{sC_{\mathrm{oss1}}}+(I_1-i_{Lr1}(s))\frac{1}{sC_{\mathrm{oss3}}}=0\\ \frac{v_{Cr1}(t_2)}{s}-L_{\mathrm{r1}}i_{Lr1}(t_2)+\frac{nV_{\mathrm{o}}}{2s}+\left(\frac{1}{sC_{\mathrm{r1}}}+sL_{\mathrm{r1}}\right)i_{Lr1}(s)\\ +(i_{Lr1}(s)-I_1)\frac{1}{sC_{\mathrm{oss3}}}=0.\end{cases} \tag{12}$$

And $v_{\mathrm{ds3}}(t_2)$ equals to V_{in}, so

$$i_{Lr1}(t) = i_{Lr1}(t_2)\cos\left[\omega_1(t-t_2)\right] - \frac{2v_{Cr1}(t_2)+nV_{\mathrm{o}}}{2Z_1}\sin\left[\omega_1(t-t_2)\right]. \tag{13}$$

The i_{Lm} is written as

$$i_{Lm}(t) = i_{Lm}(t_2) + \frac{nV_{\mathrm{o}}}{2L_{\mathrm{m}}}(t-t_2). \tag{14}$$

4) State IV [t_3, t_4]*:* In Fig. 6(d), C_{oss3} has been discharged to zero, i_{Lr1} is passing through D_3, and the D_3 and Q_4 form a short circuit, which makes u_{ab} to zero, u_{cd} is clamped in V_{o}, i_{Lr1} continues to decrease. According to Kirchhoff's law, i_{Lr1} is written as

$$\frac{v_{Cr1}(t_3)}{s} - L_{\mathrm{r1}}i_{Lr1}(t_3) + \frac{nV_{\mathrm{o}}}{2s} + \left(\frac{1}{sC_{\mathrm{r1}}} + sL_{\mathrm{r1}}\right)i_{Lr1}(s) = 0. \tag{15}$$

So, we obtain

$$i_{Lr1}(t) = i_{Lr1}(t_3)\cos\left[\omega_2(t-t_3)\right] - \frac{2v_{Cr1}(t_3)+nV_{\mathrm{o}}}{2Z_2}\sin\left[\omega_2(t-t_3)\right]. \tag{16}$$

The i_{Lm} is written as

$$i_{Lm}(t) = i_{Lm}(t_3) + \frac{nV_{\mathrm{o}}}{2L_{\mathrm{m}}}(t-t_3). \tag{17}$$

5) State V [t_4, t_5]*:* In Fig. 6(e), Q_5 and Q_8 are turned OFF, and Q_6 and Q_7 are turned ON at t_4. i_{Lr2} charges the C_{oss5} and C_{oss8} to V_{o}, and discharges the C_{oss6} and C_{oss7} to zero, so Q_6 and Q_7 are realized ZVS. C_{oss3} has been discharged to zero, so Q_3 is also realized ZVS. u_{cd} is clamped at $-V_{\mathrm{o}}$. According to Kirchhoff's law, i_{Lr1} is written as

$$\frac{v_{Cr1}(t_4)}{s} - L_{\mathrm{r1}}i_{Lr1}(t_4) - \frac{nV_{\mathrm{o}}}{2s} + \left(\frac{1}{sC_{\mathrm{r1}}} + sL_{\mathrm{r1}}\right)i_{Lr1}(s) = 0. \tag{18}$$

So, we obtain

$$i_{Lr1}(t) = i_{Lr1}(t_4)\cos\left[\omega_2(t-t_4)\right] - \frac{2v_{Cr1}(t_4)-nV_{\mathrm{o}}}{2Z_2}\sin\left[\omega_2(t-t_4)\right]. \tag{19}$$

The expression of i_{Lm} is

$$i_{Lm}(t) = i_{Lm}(t_4) - \frac{nV_{\mathrm{o}}}{2L_{\mathrm{m}}}(t-t_4). \tag{20}$$

The time period of the five modes is given by the following equation:

$$\begin{cases} t_1-t_0 = t_3-t_2 = t_6-t_5 = T_{\mathrm{d}} \\ t_2-t_1 = (2D_{\mathrm{s}}-0.5)T_{\mathrm{s}} \\ t_4-t_3 = t_5-t_4 = (0.5-D_{\mathrm{s}})T_{\mathrm{s}} - T_{\mathrm{d}}. \end{cases} \tag{21}$$

In the same way, the working mode of the second half cycle can be obtained. According to the above analysis, the PS-PWM control can enable the switches to achieve ZVS, effectively reducing switching losses.

B. Gain Calculation of the Proposed Novel PS-PWM Method

The novel PS-PWM control method can adjust the effective voltage and voltage position input into the RTM through the phase shift and variable duty cycle of the primary side switches at the same time, and then adjust the output voltage and resonant current. Through the time domain analysis method, the gain expression is derived under the premise of considering the influence of the parasitic capacitance of the switches and the dead time on the gain.

According to Section III-A, from (10), we obtain

$$|i_{Lm}(t_1)| = i_{Lm}(t_2) = \frac{V_{\mathrm{in}}(2D_{\mathrm{s}}-0.5)T_{\mathrm{s}}}{2L_{\mathrm{m}}}. \tag{22}$$

And the following can be obtained from (14) and (22):

$$i_{Lm}(t_3) = \frac{V_{\mathrm{in}}(2D_{\mathrm{s}}-0.5)T_{\mathrm{s}} + nV_{\mathrm{o}}T_{\mathrm{d}}}{2L_{\mathrm{m}}}. \tag{23}$$

Because

$$i_{Lr1}(t_1) = i_{Lm}(t_1) = -\frac{V_{\mathrm{in}}(2D_{\mathrm{s}}-0.5)T_{\mathrm{s}}}{2L_{\mathrm{m}}}. \tag{24}$$

Substituting them into (9) can be derived as

$$\begin{aligned} i_{Lr1}(t_2) = &-\frac{V_{\mathrm{in}}(2D_{\mathrm{s}}-0.5)T_{\mathrm{s}}}{2L_{\mathrm{m}}}\cos\left[\omega_2(2D_{\mathrm{s}}-0.5)T_{\mathrm{s}}\right] \\ &+\frac{V_{\mathrm{in}}-2v_{Cr1}(t_1)-nV_{\mathrm{o}}}{2Z_2}\sin\left[\omega_2(2D_{\mathrm{s}}-0.5)T_{\mathrm{s}}\right]. \end{aligned} \tag{25}$$

Bring in (13) available

$$\begin{aligned} &i_{Lr1}(t_3) \\ &= \begin{bmatrix} -\frac{V_{\mathrm{in}}(2D_{\mathrm{s}}-0.5)T_{\mathrm{s}}}{2L_{\mathrm{m}}}\cos\left[\omega_2(2D_{\mathrm{s}}-0.5)T_{\mathrm{s}}\right] \\ +\frac{V_{\mathrm{in}}-2v_{Cr1}(t_1)-nV_{\mathrm{o}}}{2Z_2}\sin\left[\omega_2(2D_{\mathrm{s}}-0.5)T_{\mathrm{s}}\right] \end{bmatrix}\cos(\omega_1T_{\mathrm{d}}) \\ &\quad -\frac{2v_{Cr1}(t_2)+nV_{\mathrm{o}}}{2Z_1}\sin(\omega_1T_{\mathrm{d}}). \end{aligned} \tag{26}$$

According to Hypothesis 1, the following can be derived:

$$\begin{aligned} &\begin{bmatrix} -\frac{V_{\mathrm{in}}(2D_{\mathrm{s}}-0.5)T_{\mathrm{s}}}{2L_{\mathrm{m}}}\cos\left[\omega_2(2D_{\mathrm{s}}-0.5)T_{\mathrm{s}}\right] \\ +\frac{V_{\mathrm{in}}-2v_{Cr1}(t_1)-nV_{\mathrm{o}}}{2Z_2}\sin\left[\omega_2(2D_{\mathrm{s}}-0.5)T_{\mathrm{s}}\right] \end{bmatrix}\cos(\omega_1T_{\mathrm{d}}) \\ &-\frac{2v_{Cr1}(t_2)+nV_{\mathrm{o}}}{2Z_1}\sin(\omega_1T_{\mathrm{d}}) = \frac{V_{\mathrm{in}}(2D_{\mathrm{s}}-0.5)T_{\mathrm{s}}+nV_{\mathrm{o}}T_{\mathrm{d}}}{2L_{\mathrm{m}}}. \end{aligned} \tag{27}$$

It can be derived from the conservation of energy

$$\begin{cases} v_{Cr1}(t_5) = -v_{Cr1}(t_0) \\ \Delta V_{Cr1} = v_{Cr1}(t_5) - v_{Cr1}(t_0) = -2v_{Cr1}(t_0) \\ = \frac{1}{C_{\mathrm{r1}}}\int_0^{\frac{T_s}{2}} i_{Lr1}(t)dt. \end{cases} \tag{28}$$

The integral in half period is solved piecewise. According to Hypothesis 3, in the period of t_3 to t_5, the average value of the primary resonance current i_{Lr1} is

$$\Delta I_{Lr1} = i_{Lr1}(t_3) - \frac{nV_{\mathrm{o}}\left[(0.5-D_{\mathrm{s}})T_{\mathrm{s}}-T_{\mathrm{d}}\right]}{4L_{\mathrm{r1}}}. \tag{29}$$

Therefore, the integral expression of i_{Lr1} is

$$\begin{aligned}\int_0^{\frac{T_\mathrm{s}}{2}} i_{Lr1}(t)dt &= \int_0^{T_\mathrm{d}} i_{Lr1}(t)dt + \int_{T_\mathrm{d}}^{T_\mathrm{d}+(2D_\mathrm{s}-0.5)T_\mathrm{s}} i_{Lr1}(t)dt\\ &\quad+\int_{T_\mathrm{d}+(2D_\mathrm{s}-0.5)T_\mathrm{s}}^{2T_\mathrm{d}+(2D_\mathrm{s}-0.5)T_\mathrm{s}} i_{Lr1}(t)dt+\int_{2T_\mathrm{d}+(2D_\mathrm{s}-0.5)T_\mathrm{s}}^{\frac{T_\mathrm{s}}{2}} \Delta I_{Lr1}dt\\ &= \int_0^{T_\mathrm{d}} \frac{nV_\mathrm{o}(t-T_\mathrm{d})}{2L_\mathrm{m}} - \frac{V_\mathrm{in}(2D_\mathrm{s}-0.5)T_\mathrm{s}}{2L_\mathrm{m}}dt+\\ &\quad\int_{T_\mathrm{d}}^{T_\mathrm{d}+(2D_\mathrm{s}-0.5)T_\mathrm{s}} \frac{i_{Lr1}(t_1)+i_{Lr1}(t_2)}{2}\\ &\quad+\int_{T_\mathrm{d}+(2D_\mathrm{s}-0.5)T_\mathrm{s}}^{2T_\mathrm{d}+(2D_\mathrm{s}-0.5)T_\mathrm{s}} \frac{i_{Lr1}(t_2)+i_{Lm}(t_3)}{2}dt\\ &\quad+\int_{2T_\mathrm{d}+(2D_\mathrm{s}-0.5)T_\mathrm{s}}^{\frac{T_\mathrm{s}}{2}} i_{Lm}(t_3) - \frac{nV_\mathrm{o}[(0.5-D_\mathrm{s})T_\mathrm{s}-T_\mathrm{d}]}{4L_\mathrm{r1}}dt.\end{aligned} \tag{30}$$

And because

$$\begin{aligned}&v_{Cr1}(t_1)\\ &= v_{Cr1}(t_0)+\frac{1}{C_\mathrm{r1}}\int_0^{T_\mathrm{d}}\left(\frac{nV_\mathrm{o}(t-T_\mathrm{d})}{2L_\mathrm{m}}-\frac{V_\mathrm{in}(2D_\mathrm{s}-0.5)T_\mathrm{s}}{2L_\mathrm{m}}\right)dt\end{aligned} \tag{31}$$

$$\begin{aligned}&v_{Cr1}(t_2)\\ &= v_{Cr1}(t_1)+\frac{1}{C_\mathrm{r1}}\int_{T_\mathrm{d}}^{T_\mathrm{d}+(2D_\mathrm{s}-0.5)T_\mathrm{s}}\frac{i_{Lr1}(t_1)+i_{Lr1}(t_2)}{2}dt.\end{aligned} \tag{32}$$

According to Hypothesis 2, the following can be derived from the conservation of charge:

$$\begin{aligned}&\int_{T_\mathrm{d}+(2D_\mathrm{s}-0.5)T_\mathrm{s}}^{2T_\mathrm{d}+(2D_\mathrm{s}-0.5)T_\mathrm{s}} i_{Lr1}(t)dt\\ &= \int_{T_\mathrm{d}+(2D_\mathrm{s}-0.5)T_\mathrm{s}}^{2T_\mathrm{d}+(2D_\mathrm{s}-0.5)T_\mathrm{s}} \frac{i_{Lr1}(t_2)+i_{Lm}(t_3)}{2}dt = 2\mathrm{C}_\mathrm{oss}V_\mathrm{in}.\end{aligned} \tag{33}$$

According to (24)–(26) and (29)–(33), the voltage gain G expression can be derived as

$$G=\frac{nV_\mathrm{o}}{V_\mathrm{in}}=\frac{\left[\begin{array}{l}\frac{(2D_\mathrm{s}-0.5)T_\mathrm{s}\{\cos[\omega_2(2D_\mathrm{s}-0.5)T_\mathrm{s}]-1\}}{2L_\mathrm{m}}+\frac{4\mathrm{C}_\mathrm{oss}}{T_\mathrm{d}}\\ -\frac{(1-2\boldsymbol{A})\sin[\omega_2(2D_\mathrm{s}-0.5)T_\mathrm{s}]}{2Z_2}\end{array}\right]}{\frac{T_\mathrm{d}}{2L_\mathrm{m}}-\frac{(1+\boldsymbol{B})\sin[\omega_2(2D_\mathrm{s}-0.5)T_\mathrm{s}]}{Z_2}}. \tag{34}$$

Of which

$$\begin{aligned}&\boldsymbol{A}\\ &=\left(\frac{(2D_\mathrm{s}-0.5)T_\mathrm{s}[(2D_\mathrm{s}-0.5)T_\mathrm{s}+T_\mathrm{d}]\cos[\omega_2(2D_\mathrm{s}-0.5)T_\mathrm{s}]}{8L_\mathrm{m}C_\mathrm{r1}}\right.\\ &+\frac{(2D_\mathrm{s}-0.5)^2T_\mathrm{s}^2}{8L_\mathrm{m}C_\mathrm{r1}}-\frac{[(2D_\mathrm{s}-0.5)T_\mathrm{s}+T_\mathrm{d}]\sin[\omega_2(2D_\mathrm{s}-0.5)T_\mathrm{s}]}{8Z_2C_\mathrm{r1}}\\ &\left.-\frac{(2D_\mathrm{s}-0.5)T_\mathrm{s}[(1-2D_\mathrm{s})T_\mathrm{s}-2T_\mathrm{d}]}{4L_\mathrm{m}C_\mathrm{r1}}-\frac{3(2D_\mathrm{s}-0.5)T_\mathrm{s}T_\mathrm{d}}{8L_\mathrm{m}C_\mathrm{r1}}\right)\\ &\times\frac{4Z_2C_\mathrm{r1}}{4Z_2C_\mathrm{r1}-[(2D_\mathrm{s}-0.5)T_\mathrm{s}+T_\mathrm{d}]\sin[\omega_2(2D_\mathrm{s}-0.5)T_\mathrm{s}]}\end{aligned} \tag{35}$$

$$\begin{aligned}&\boldsymbol{B}=\\ &\left(-\frac{T_\mathrm{d}^2+T_\mathrm{d}[(1-2D_\mathrm{s})T_\mathrm{s}-2T_\mathrm{d}]}{4L_\mathrm{m}C_\mathrm{r1}}+\frac{[(2D_\mathrm{s}-0.5)T_\mathrm{s}+T_\mathrm{d}]\sin[\omega_2(2D_\mathrm{s}-0.5)T_\mathrm{s}]}{8Z_2C_\mathrm{r1}}\right.\\ &\left.+\frac{[(0.5-D_\mathrm{s})T_\mathrm{s}-T_\mathrm{d}]^2}{4L_\mathrm{r1}C_\mathrm{r1}}\right)\frac{4Z_2C_\mathrm{r1}}{4Z_2C_\mathrm{r1}-[(2D_\mathrm{s}-0.5)T_\mathrm{s}+T_\mathrm{d}]\sin[\omega_2(2D_\mathrm{s}-0.5)T_\mathrm{s}]}.\end{aligned} \tag{36}$$

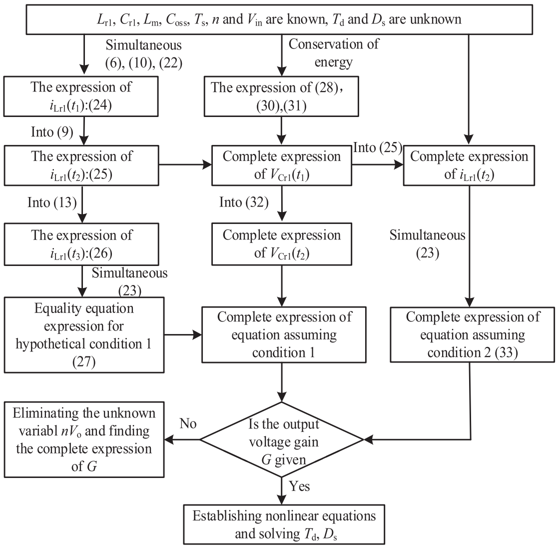

Fig. 7. Flowchart of the calculation steps.

TABLE I
PARAMETERS OF SIMULATION EXPERIMENT

Simulation parameters	Values
V_in	200 V
V_o	200 V
P_o	800 W
C_r1&C_r2	78.56 nF:78.56 nF
L_r1&L_r2	32.25 μH:32.25 μH
L_m	167.7 μH
TX	1:1
R_L	1000 Ω
f_s	100 KHz
C_o	940 μF
C_oss	553 pF

The voltage gain G is not only related to D_s but also related to T_d. When G is known, that is, nV_o is known, the circuit parameters and the expressions of $v_{\mathrm{cr1}}(t_1)$ and $v_{\mathrm{cr1}}(t_2)$ (30)–(32) can be substituted into (27) and (33) to obtain the required D_s and T_d. The flowchart of the calculation steps is shown in Fig. 7.

IV. SIMULATION VERIFICATION AND ANALYSIS

In order to verify the effectiveness and practicability of the proposed novel PS-PWM control method, the design prototype parameters are shown in Table I. Usually, the range of Q is 0–1 and k is 2.5–6 in *CLLC* resonator design. The design of resonator parameters mainly refers [12]. In [12], $k = 4.3$, $Q = 0.52$; therefore, this article takes $k = 5.2$, $Q = 0.5$. Because the application scenario assumed in this article is large-capacity uninterruptible power supply, this kind of power needs 24 h uninterrupted work, the rated power is about 800 W, so this article sets the rated power 800 W, resonant frequency 100 KHz.

The above-mentioned parameters are substituted into the voltage gain G (D_s, T_d), and then the function curves of G (D_s, T_d) are drawn by Mathcad as shown in Fig. 8(a). It can be seen that G decreases with the decrease of D_s, so this method can effectively adjust the gain; when D_s is fixed, G slowly increases

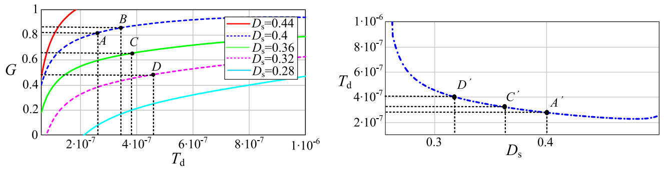

(a) (b)

Fig. 8. (a) Function curves of G (D_s, T_d). (b) Relationship curve of T_d (D_s).

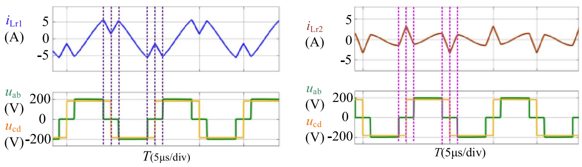

(a) (b)

Fig. 9. Simulation waveforms. (a) u_ab, u_cd, i_{Lr1}. (b) u_ab, u_cd , i_{Lr2}.

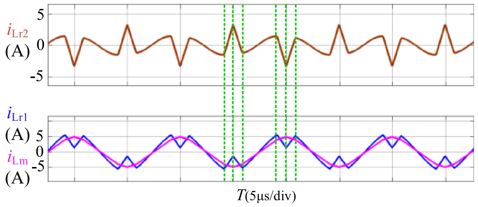

Fig. 10. Simulation waveform: i_{Lr1}, i_{Lm}, i_{Lr2}.

with the increase of T_d, indicating that T_d will affect G of the *CLLC* resonant converter under light-load conditions. The above-mentioned parameters are substituted into (33), and we can get the implicit function $f\,(D_\text{s}, T_\text{d}) = 0$ of D_s and T_d when the switches are realized critical ZVS. The relationship curve of T_d (D_s) is shown in Fig. 8(b).

The main parameters of the simulation circuit in MATLAB are shown in Table I. Under the condition of 5% load, the novel PS-PWM control method is used to control the converter. When D_s is 0.4, it is obtained that T_d is 287 ns, which is point A' shown in Fig. 8(b). When V_in is 200 V, the simulation waveforms of u_ab, u_cd, and i_{Lr1} are shown in Fig. 9(a). The simulation waveforms of u_ab, u_cd, and i_{Lr2} are shown in Fig. 9(b). The simulated waveforms of i_{Lr1}, i_{Lm}, and i_{Lr2} are shown in Fig. 10. The simulation waveforms in Figs. 9 and 10 are basically consistent with those in Fig. 5, and the circuit realizes the purpose of reducing the equivalent duty cycle of the RTM input to reduce the voltage gain and reducing the current stress.

The soft switching of the switches is shown in Fig. 11. It can be seen that both the primary side and the secondary side can realize ZVS, which effectively reduces the losses of the switches and improves the power transmission efficiency.

The input and output voltage waveforms are shown in Fig. 12. When V_in is 200 V and the transformer ratio is 2:1, the V_o is 85 V, that is, the voltage gain is 0.85, which realizes the purpose of light load and low gain output. And the calculated result G is 0.829, which is point A' shown in Fig. 8(a), and the results are basically consistent with the simulation results.

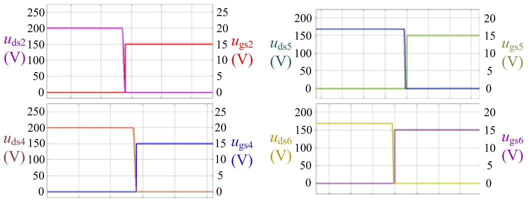

(a) (b)

Fig. 11. ZVS simulation waveforms of switches. (a) Primary side switches. (b) Secondary side switches.

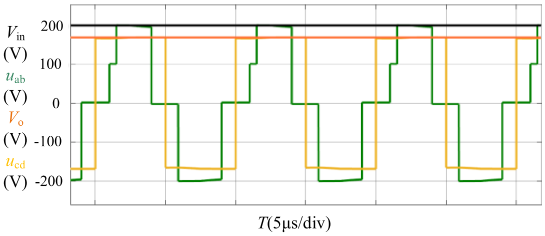

Fig. 12. Simulation waveform: V_in, V_o, u_ab, u_cd..

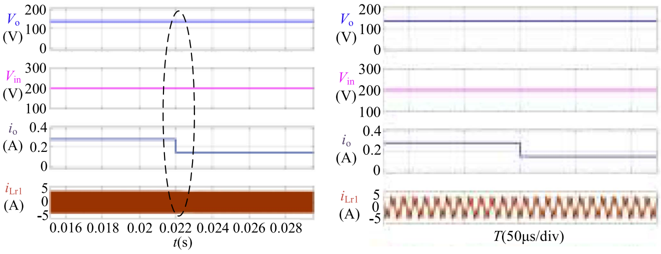

Fig. 13. Simulation waveforms: V_in, V_o, i_o, i_{Lr1} simulation waveform.

When V_o is constant at 140 V and the load is switched from the original 10% load to 5% load, the transformation waveforms of V_in, V_o, i_o, and i_{Lr1} are shown in Fig. 13.

It can be seen that V_o remains constant before and after switching load, whereas i_o is halved and i_{Lr1} is slightly reduced. So, V_o can be kept constant under different loads.

The simulation results further show that the novel PS-PWM control method can effectively reduce the voltage gain of the *CLLC* resonant converter under light-load conditions. And it can also realize the ZVS of switches and make the converter have higher power transmission efficiency.

V. EXPERIMENTAL VERIFICATION AND ANALYSIS

In order to further verify the correctness of the proposed control method, there is an experimental prototype with V_in of 200 V, V_o of 200 V, f_s of 100 kHz, and the rated power of 800 W built, which is shown in Fig. 14.

The parameters of the prototype are the same as the simulation, and the specific device specifications are supplemented, as shown in Table II.

Since this control method is applied to the *CLLC* resonant converter under light-load conditions, the experimental conditions are chosen to be carried out under 5% load.

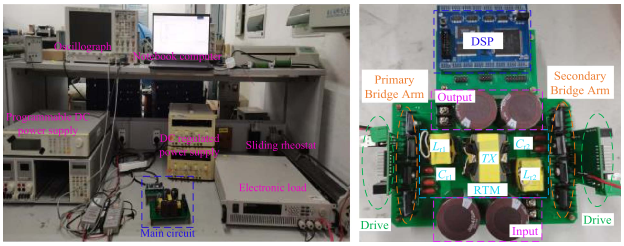

Fig. 14. Experimental prototype.

TABLE II
COMPONENTS TABLE OF THE PROTOTYPE

Device	Specification selection
Q_1–Q_8	NTHL110N65S3F(650 V/30 A) $R_{\mathrm{DS(on),typ}}$=98 mΩ, C_{oss}=553 pF
DSP	TI TMS320F28335
TX	Ferrite PQ40
L_{r1}/L_{r2}	Ferrite PQ2625
C_{r1}/C_{r2}	CBB22 630 V
C_{in}/C_{o}	ECAP 500 V/470 μf

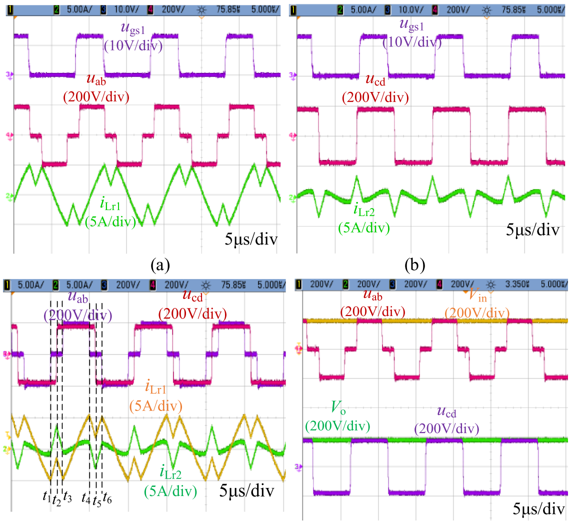

(a) (b)

(c) (d)

Fig. 15. Experimental waveforms. (a) u_{ab}, u_{gs1}, i_{Lr1}. (b) u_{gs1}, u_{cd}, i_{Lr2}. (c) u_{ab}, u_{cd}, i_{Lr1} , i_{Lr2}. (d) u_{ab}, u_{cd}, V_{in} , V_{o}.

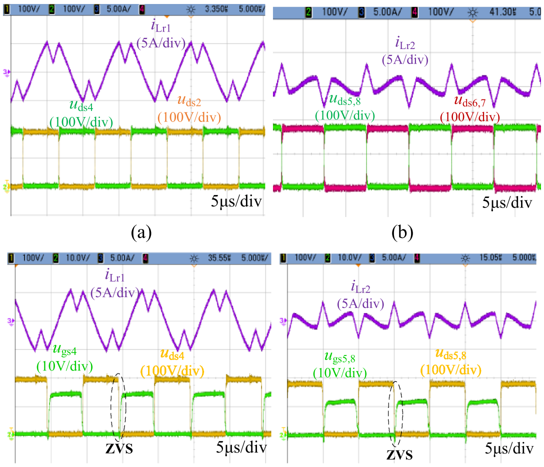

(a) (b)

(c) (d)

Fig. 16. Experimental waveforms. (a) i_{Lr1}, u_{ds2}, u_{ds4}. (b) i_{Lr2}, $u_{\mathrm{ds5,8}}$, $u_{\mathrm{ds6,7}}$. (c) i_{Lr1}, u_{ds4}, u_{gs4}. (d) i_{Lr2}, u_{ds5}, u_{gs5}.

The experimental waveforms of u_{ab}, u_{gs1}, and i_{Lr1} are shown in Fig. 15(a). The output voltage is adjusted by changing the duty cycle of the input voltage of the RTM, and the change of i_{Lr1} corresponding to u_{ab} is basically consistent with the transient analysis in Section III-A. The variation of i_{Lr2} with u_{gs1} and u_{cd} is shown in Fig. 15(b). The waveforms of input and output voltage of the RTM and resonant current are shown in Fig. 15(c). And the time period for transmitting energy from the output side to the input side in each cycle is divided into two small segments t_1–t_3 and t_4–t_6 on average to slow down the change of the resonant current during this period. $I_{\mathrm{Lr1\cdot rms}} = 3.18$ A, $I_{\mathrm{Lr2\cdot rms}} = 1.34$ A and $I_{\mathrm{Lr1\cdot peak}} = 5.21$ A and $I_{\mathrm{Lr2\cdot peak}} = 3.29$ A were measured. The experimental waveforms of u_{ab}, u_{cd} and V_{in}, V_{o} are shown in Fig. 15(d). Due to certain interference and loss in the experimental circuit, T_{d} should be set larger than the calculated value, and its value is 340 ns, which is point *B* shown in Fig. 8(a). The experimental gain is 0.9 and the calculated gain is 0.855, which are basically consistent.

The experimental waveforms of i_{Lr1} and u_{ds2}, u_{ds4} of the primary side switches Q_2, Q_4 are shown in Fig. 16(a). It can be seen that $i_{Lr1}<0$ before Q_4 is turned ON and $i_{Lr1}>0$ before Q_2 is turned ON, so Q_2 and Q_4 are realized ZVS. Similarly, Q_1 and Q_3 are also realized ZVS. The experimental waveforms of i_{Lr2} and $u_{\mathrm{ds5,8}}$, $u_{\mathrm{ds6,7}}$ of the secondary side switches $Q_{5,8}$, $Q_{6,7}$ are shown in Fig. 16(b). It can be seen that $i_{\mathrm{Lr2}}>0$ before $Q_{5,\ 8}$ are turned ON, and $i_{\mathrm{Lr2}}<0$ before $Q_{6,7}$ are turned ON, so $Q_{5,8}$ and $Q_{6,7}$ are realized ZVS. The experimental waveforms of i_{Lr1} and u_{gs4}, u_{ds4} of the primary side switch Q_4 are shown in Fig. 16(c). It can be seen that Q_4 is realized ZVS when $i_{Lr1}<0$. The experimental waveforms of i_{Lr2} and u_{gs5}, u_{ds5} of the secondary side switch Q_5 are shown in Fig. 16(d). It can be seen that when $i_{Lr2}>0$, Q_5 is realized ZVS. Therefore, both the primary and secondary side switches are realized ZVS, which can effectively reduce the losses of the switches and improve the transmission efficiency of the circuit.

In order to verify the accuracy of the gain curves in Fig. 8(a), the voltage gain values when D_{s} are 0.36 and 0.32 are also measured. When D_{s} is 0.36, T_{d} is 315 ns, which is shown at C' in Fig. 8(b). However, due to some interference and loss in the experimental circuit, T_{d} needs to be set larger than the calculated value, so T_{d} is set to 380 ns. Therefore, the calculated gain is shown at *C* in Fig. 8(a), and the calculated result *G* is 0.652. The experimental waveforms at D_{s} of 0.36 are shown in Fig. 17(a) and (b), and the voltage gain obtained from the experiment is 0.7, which is basically consistent with the calculation results.

When D_{s} is 0.32, T_{d} is 403 ns, which is shown at D' in Fig. 8(b). In the experiment, T_{d} is actually set to 460 ns. Therefore, the calculated gain is shown at *D* in Fig. 8(a), and the calculated result *G* is 0.491. The experimental waveforms at D_{s} of 0.32 are shown in Fig. 17(c) and (d), and the voltage

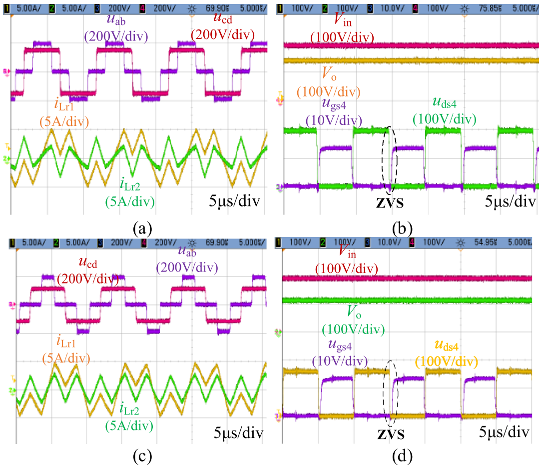

Fig. 17. Experimental waveforms. (a) D_s=0.36 u_{ab}, u_{cd}, i_{Lr1}, i_{Lr2}. (b) D_s=0.36 V_{in}, V_o, u_{ds4}, u_{gs4}. (c) D_s=0.32 u_{ab}, u_{cd}, i_{Lr1}, i_{Lr2}. (d) D_s=0.32 V_{in}, V_o, u_{ds4}, u_{gs4}.

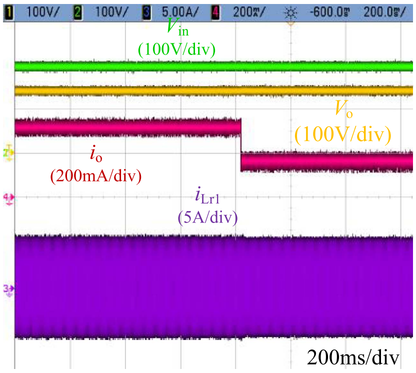

Fig. 18. Experimental waveforms: V_{in}, V_o, i_o, i_{Lr1}.

gain obtained from the experiment is 0.55, which is basically consistent with the calculation results.

When V_o is constant at 140 V and the load is switched from the original 10% load to 5% load, the transformation waveforms of V_{in}, V_o, i_o, and i_{Lr1} are shown in Fig. 18.

It can be seen that V_o remains constant before and after load switching, whereas i_o is halved and i_{Lr1} is slightly reduced. It is basically consistent with the simulation results, which proves that V_o can remain constant under different loads.

The experimental key waveforms of APWM are shown in Fig. 19. When $G = 0.9$, the waveforms of input and output voltage of the RTM and resonant current are shown in Fig. 19(a). The fundamental phase of the voltage at the midpoint of the bridge arm on both sides of the voltage transformer is not the same, and the time period for transmitting energy from the output side to the input side in each cycle is t_1–t_3, which makes the resonant current change greatly during this time. $I_{Lr1\_rms} = 1.93$ A, $I_{Lr2\_rms} = 2.34$ A and $I_{Lr1\_peak} = 3.97$ A and $I_{Lr2\_peak} = 7.13$ A were measured. The stress of the primary switches is slightly smaller than that of the PS-PWM, but the stress of the secondary switches is much larger than that of the PS-PWM control. That the control can make the primary and secondary switches achieve ZVS are shown in Fig. 19(b) and (c). However, when $i_{Lr2} = I_{Lr2\_peak}$, the $Q_{5,8}$ are in the turn-OFF stage, which will lead to a sharp increase in the turn-OFF losses of the switches. When $G = 0.55$, the waveforms of input and output voltage of the RTM and resonant current are shown in Fig. 19(d). At this time, the measured $I_{Lr1\_rms} = 2.91$ A, $I_{Lr2\_rms} = 3.02$ A and $I_{Lr1\_peak} = 5.02$ A and $I_{Lr2\_peak} = 7.98$ A, I_{Lr_rms} and I_{Lr_peak} are increased. And the stress of primary and secondary switches and I_{Lr_rms} of APWM control are greater than those of PS-PWM control, which leads to the efficiency of APWM is less than that of PS-PWM, and with the decrease of gain, the efficiency of PS-PWM will be more and more greater than that of APWM.

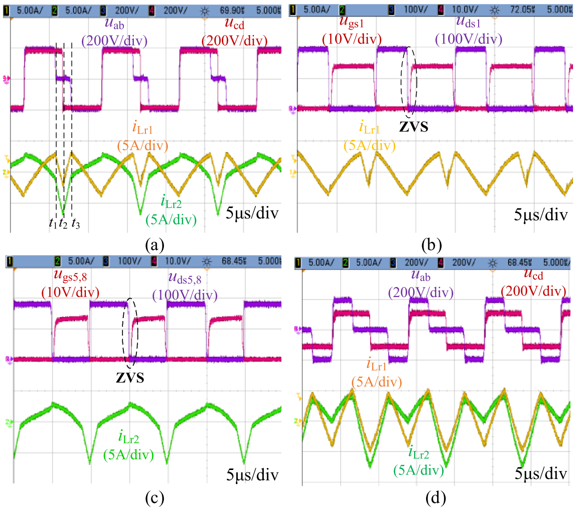

Fig. 19. Experimental waveforms of APWM. (a) G=0.9 u_{ab}, u_{cd}, i_{Lr1}, i_{Lr2}. (b) G=0.9 i_{Lr1}, u_{ds4}, u_{gs4}. (c) G=0.9 i_{Lr2}, $u_{ds5,8}$, $u_{gs5,8}$. (d) G=0.55 u_{ab}, u_{cd}, i_{Lr1}, i_{Lr2}.

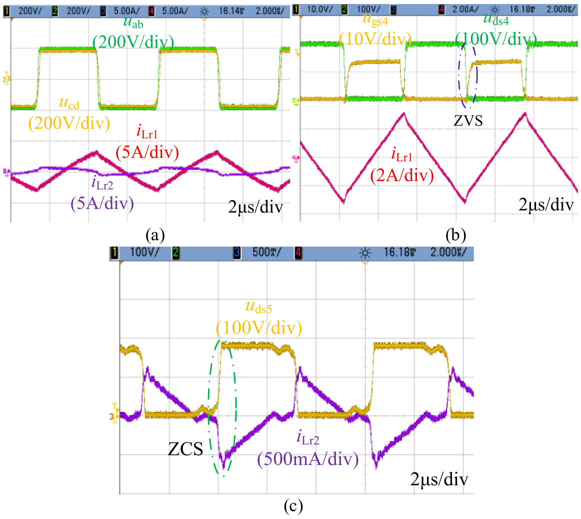

Fig. 20. Experimental waveforms of PFM. (a) u_{ab}, u_{cd}, i_{Lr1}, i_{Lr2}.. (b) i_{Lr1}, u_{ds4}, u_{gs4}. (c) i_{Lr2}, u_{ds5}.

The experimental key waveforms of PFM are shown in Fig. 20. When $f_n = 1.6$, the waveforms of input and output voltage of the RTM and resonant current are shown in Fig. 20(a). PFM control is difficult to achieve low voltage gain under light load. At this time, if the frequency modulation control is continued, the switching frequency will continue to rise, even

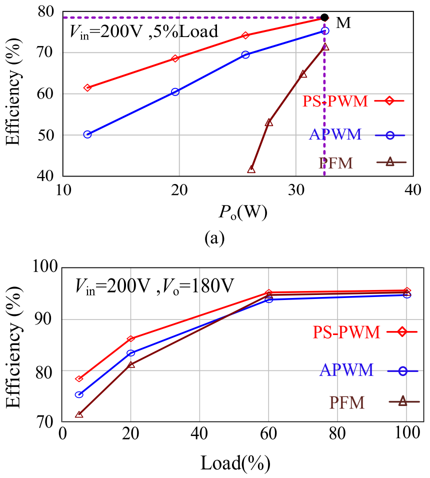

(a)

(b)

Fig. 21. Efficiency curves of different control. (a) $V_{\rm in}$ =200 V, 5% load. (b) $V_{\rm in}$ =200 V, $V_{\rm o}$ =180 V.

exceeding the upper limit of frequency. Not only the output voltage will deviate from the reference value, but also lead to great switching loss and extremely low transmission efficiency. That the control can make the primary side of the switches achieve ZVS but the secondary side of the switches in the realization of ZCS will produce a certain loss are shown in Fig. 20(b) and (c).

The efficiency curves of the three control methods at 5% load are shown in Fig. 21(a). It can be seen that as the output power decreases, that is, the output voltage decreases, the efficiency of PS-PWM control is more and more greater than that of APWM control. PFM control cannot effectively reduce the output voltage, and the transmission efficiency is extremely low. The efficiency curves of the three control modes in the full load range when $V_{\rm o}$ = 180 V are shown in Fig. 21(b). At full load and heavy load, the efficiency of the three control methods is not much different, but as the load decreases, the efficiency of PS-PWM will be more and more greater than that of APWM and PFM.

Actually, the converter will generate the following.

1) Transformer losses $P_{\rm TX}$.
2) Resonant inductor losses $P_{\rm Lr1}$, $P_{\rm Lr2}$.
3) Switching losses of MOSFETs that mainly refer to turn-OFF losses $P_{\rm off}$ of switches since realizing of ZVS.
4) Conduction losses $P_{\rm on}$ of switches.

Then, the pie charts are plotted to show the theoretical power losses distribution and efficiency of the prototype on output power $P_{\rm rate}$ = 32.4 W when the working condition is 5% light load, as shown in Fig. 22.

There is a small error between experimental efficiency shown at point M in Fig. 21(a) and theoretical efficiency, which may be due to calculation errors and the presence of equivalent impedance due to printed circuit board (PCB) layout or component differences.

Based on the above experimental analysis, when the bidirectional full-bridge *CLLC* resonant converter under light-load conditions, the novel PS-PWM control method can not only effectively adjust the voltage gain but also achieve high output efficiency.

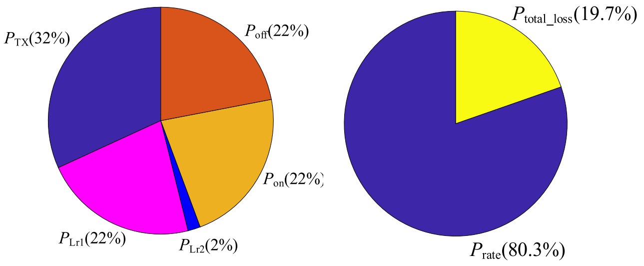

Fig. 22. Theoretical power losses distribution and efficiency of the prototype.

VI. CONCLUSION

Aiming at the improvement of problems of voltage gain imbalance and low energy transmission efficiency in PFM control of bidirectional full-bridge *CLLC* resonant converter under light-load conditions, a novel PS-PWM control method is proposed, which can flexibly adjust the voltage gain by adjusting the duty cycle $D_{\rm s}$ and the original edge shift phase angle. At the same time, this control can make the primary side and secondary side switches achieve ZVS, and solve the problem that the duty cycle is limited by soft switching in PWM control. Moreover, the current stress of switches controlled by PS-PWM is smaller than that controlled by APWM, which can reduce the loss of switches and improve the energy transmission efficiency of the converter. Finally, considering the parasitic parameters and dead time of the switches, the voltage gain of the proposed control method under light load is precise research by using the time domain analysis method. The simulation and experimental results both show that the control method solves the problem of light-load voltage gain imbalance and low efficiency of bidirectional full-bridge *CLLC* resonant converter.

REFERENCES

[1] B. Zhao, Q. Song, W. Liu, and Y. Sun, "Overview of dual-active-bridge isolated bidirectional DC–DC converter for high-frequency-link power-conversion system," *IEEE Trans. Power Electron.*, vol. 29, no. 8, pp. 4091–4106, Aug. 2014.

[2] T. Jin and W. Zhang, "A novel interpolated DFT synchrophasor estimation algorithm with an optimized combined cosine self-convolution window," *IEEE Trans. Instrum. Meas.*, vol. 70, 2021, Art. no. 9000610.

[3] P. He, A. Mallik, A. Sankar, and A. Khaligh, "Design of a 1-MHz high-efficiency high-power-density bidirectional GaN-based CLLC converter for electric vehicles," *IEEE Trans. Veh. Technol.*, vol. 68, no. 1, pp. 213–223, Jan. 2019.

[4] V. V. Reddy P., H. M. Suryawanshi, G. G. Talapur, and M. S. Ballal, "Optimized resonant converter by implementing shunt branch element as magnetizing inductance of transformer in electric vehicle chargers," *IEEE Trans. Ind. Appl.*, vol. 55, no. 6, pp. 7471–7480, Nov./Dec. 2019.

[5] T. Jin, Y. Huang, Y. Lin, and M. N. Daniel Legrand, "Model predictive current control based on virtual voltage vector method for parallel three-level inverters," *IEEE Trans. Emerg. Sel. Topics Power Electron.*, vol. 9, no. 5, pp. 6049–6058, Oct. 2021.

[6] H. V. Nguyen, D. C. Lee, and F. Blaabjerg, "A novel SiC-based multifunctional onboard battery charger for plug-in electric vehicles," *IEEE Trans. Power Electron.*, vol. 36, no. 5, pp. 5635–5646, May 2021.

[7] T. Y. Jiang, J. M. Zhang, X. K. Wu, K. Sheng, and Y. Wang, "A bidirectional LLC resonant converter with automatic forward and backward mode transition," *IEEE Trans. Power Electron.*, vol. 30, no. 2, pp. 757–770, Feb. 2015.
[8] S. S. Shah, S. K. Rastogi, and S. Bhattacharya, "Paralleling of LLC resonant converters," *IEEE Trans. Power Electron.*, vol. 36, no. 6, pp. 6276–6287, Jun. 2021.
[9] Z. M. Dalala, Z. U. Zahid, O. S. Saadeh, and J. S. Lai, "Modeling and controller design of a bidirectional resonant converter battery charger," *IEEE Access*, vol. 6, pp. 23338–23350, 2018.
[10] A. Sankar, A. Mallik, and A. Khaligh, "Extended harmonics based phase tracking for synchronous rectification in CLLC converters," *IEEE Trans. Ind. Electron.*, vol. 66, no. 8, pp. 6592–6603, Aug. 2019.
[11] S. Zou, J. Lu, A. Mallik, and A. Khaligh, "Bi-directional CLLC converter with synchronous rectification for plug-in electric vehicles," *IEEE Trans. Ind. Appl.*, vol. 54, no. 2, pp. 998–1005, Mar./Apr. 2018.
[12] J. Jung, H. Kim, M. Ryu, and J. Baek, "Design methodology of bidirectional CLLC resonant converter for high-frequency isolation of DC distribution systems," *IEEE Trans. Power Electron.*, vol. 28, no. 4, pp. 1741–1755, Apr. 2013.
[13] T. Zhu, F. Zhuo, F. Zhao, F. Wang, H. Yi, and T. Zhao, "Optimization of extended phase-shift control for full-bridge CLLC resonant converter with improved light-load efficiency," *IEEE Trans. Power Electron.*, vol. 35, no. 10, pp. 11129–11142, Oct. 2020.
[14] J. Kim, C. Kim, J. Kim, J. Lee, and G. Moon, "Analysis on load-adaptive phase-shift control for high efficiency full-bridge LLC resonant converter under light-load conditions," *IEEE Trans. Power Electron.*, vol. 31, no. 7, pp. 4942–4955, Jul. 2016.
[15] S. A. Arshadi, M. Ordonez, W. Eberle, M. Craciun, and C. Botting, "Three-phase LLC battery charger: Wide regulation and improved light-load operation," *IEEE Trans. Power Electron.*, vol. 36, no. 2, pp. 1519–1531, Feb. 2021.
[16] A. Awasthi, S. Bagawade, and P. K. Jain, "Analysis of a hybrid variable-frequency-duty-cycle-modulated low-Q LLC resonant converter for improving the light-load efficiency for a wide input voltage range," *IEEE Trans. Power Electron.*, vol. 36, no. 7, pp. 8476–8493, Jul. 2021.
[17] W. Feng, F. C. Lee, and P. Mattavelli, "Optimal trajectory control of burst mode for LLC resonant converter," *IEEE Trans. Power Electron.*, vol. 28, no. 1, pp. 457–466, Jan. 2013.
[18] C. Fei, Q. Li, and F. C. Lee, "Digital implementation of light-load efficiency improvement for high-frequency LLC converters with simplified optimal trajectory control," *IEEE Trans. Emerg. Sel. Topics Power Electron.*, vol. 6, no. 4, pp. 1850–1859, Dec. 2018.
[19] Z. Fang et al., "Energy feedback control of light-load voltage regulation for LLC resonant converter," *IEEE Trans. Power Electron.*, vol. 34, no. 5, pp. 4807–4819, May 2019.
[20] H. Pan, C. He, F. Ajmal, H. Chen, and G. Chen, "Pulse-width modulation control strategy for high efficiency LLC resonant converter with light load applications," *IET Power Electron.*, vol. 7, no. 11, pp. 2887–2894, Nov. 2014.
[21] W. Cha, J. Kwon, and B. Kwon, "Highly efficient asymmetrical PWM full-bridge converter for renewable energy sources," *IEEE Trans. Ind. Electron.*, vol. 63, no. 5, pp. 2945–2953, May 2016.
[22] T. Zhu, F. Zhuo, F. Zhao, K. Yu, F. Wang, and R. Song, "A novel APWM control scheme for GaN based full-bridge CLLC resonant converter with improved light-load efficiency," in *Proc. IEEE Appl. Power Electron. Conf. Expo.*, 2020, pp. 2081–2085.
[23] S. M. S. I. Shakib and S. Mekhilef, "A frequency adaptive phase shift modulation control based LLC series resonant converter for wide input voltage applications," *IEEE Trans. Power Electron.*, vol. 32, no. 11, pp. 8360–8370, Nov. 2017.
[24] B. Li, M. Chen, X. Wang, N. Chen, X. Sun, and D. Zhang, "An optimized digital synchronous rectification scheme based on time-domain model of resonant CLLC circuit," *IEEE Trans. Power Electron.*, vol. 36, no. 9, pp. 10933–10948, Sep. 2021.
[25] J. Sun, L. Yuan, Q. Gu, R. Duan, Z. Lu, and Z. Zhao, "Design-oriented comprehensive time-domain model for CLLC class isolated bidirectional DC-DC converter for various operation modes," *IEEE Trans. Power Electron.*, vol. 35, no. 4, pp. 3491–3505, Apr. 2020.
[26] L. Zhao, Y. Pei, L. Wang, L. Pei, W. Cao, and Y. Gan, "Design methodology of bidirectional resonant CLLC charger for wide voltage range based on parameter equivalent and time domain model," *IEEE Trans. Power Electron.*, vol. 37, no. 10, pp. 12041–12064, Oct. 2022.

Yuzhen Xu was born in Jiangxi Province, China, in 1975. She received the B.S. degree in electric power system and automation, M.S. degree in control theory and control engineering, and Ph.D. degree in motors and electrical from Fuzhou University, Fuzhou, China, in 1998, 2001, and 2007, respectively.

She was an Associate Professor with the College of Electrical Engineering and Automation, Fuzhou University. Her research interests include power electronic converter topology derivation and control technology and LED lighting technology. In these areas, she had authored/coauthored dozens of papers and patents for inventions.

Xiangyang Dai was born in Anhui Province, China, in 1996. He received the B.S. degree in electrical engineering and automation from Heilongjiang University of Science and Technology, Harbin, China, in 2020. Since 2020, he has been working toward the M.S. degree in power electronics and power transmission with the Department of Electrical Engineering and Automation, Fuzhou University, Fuzhou, China.

His research interests include the power converter technology for power electronics, new energy generation, and energy routers.

Zhongyi Zhang was born in Jiangxi Province, China, in 1993. He received the M.S. degree in electrical engineering and automation from East China Jiaotong University, Nanchang, China, in 2020. Since September 2020, he has been working toward the Ph.D. degree in electrical engineering with the Department of Electrical Engineering and Automation, Fuzhou University, Fuzhou, China.

His current research is major for the dc–dc converter topology derivation and related modeling and control technology focused on distributed new energy power supply system.

Zhiwei Kang was born in Fujian Province, China, in 1998. He received the B.S. degree in electrical engineering and automation from Minnan Normal University, Zhangzhou, China, in 2020. Since 2020, he has been working toward the M.S. degree in electrical engineering with the Departmentof Electrical Engineering and Automation, Fuzhou University, Fuzhou, China.

He research interests include the power converter technology for power electronics, new energy generation, and energy routers.

Tao Jin (Senior Member, IEEE) received the B.S. and M.S. degrees in electrical engineering from Yanshan University, Qinhuangdao, China, in 1998 and 2001, respectively, and the Ph.D. degree in electrical engineering from Shanghai Jiao Tong University, Shanghai, China, in 2005.

From 2005 to 2007, he was a Postdoctor with Shanghai Jiao Tong University. During this time, he was in charge of a research group in the biggest dry-type transformer company in Asia, Sunten Electrical Co. Ltd., to develop new transformer technology with distribution grid. From 2008 to 2009, he was a Research Scientist with Virginia Tech, Blacksburg, VA, USA, where he was involved in the design and test of PMU technology and GPS/Internet-based power system frequency monitoring network. In 2010, he joined, as a European Union Marie Curie Research Fellow, Imperial College London, London, U.K., where he was focused on electrical technologies related to smart grid. He is currently a Professor with the College of Electrical Engineering and Automation, Fuzhou University, Fuzhou, China. He authored/coauthored about 180 papers.

Dr. Jin is a member of the IEEE Power and Energy Society and IEEE Industrial Electronics Society, and a special committee member of the Chinese Society of Electrical Engineering, China Electrotechnical Society, etc. He is currently an Associate Editor for *Journal of Modern Power Systems and Clean Energy*, *Protection and Control of Modern Power Systems*, *China Measurement and Testing Technology*, and other journals.